

Solar energetic particle event and radio bursts associated with the 1996 July 9 flare and coronal mass ejection

T. Laitinen¹, K.-L. Klein², L. Kocharov¹, J. Torsti¹, G. Trottet², V. Bothmer³, M.L. Kaiser⁴, G. Rank⁵, and M.J. Reiner⁶

¹ Space Research Laboratory, Department of Physics, University of Turku, 20014 Turku, Finland

² Observatoire de Paris, Section de Meudon, DASOP & CNRS UMR 8645, 92195 Meudon, France

³ Institut für Experimentelle und Angewandte Physik, Universität Kiel, 24118 Kiel, Germany

⁴ Goddard Space Flight Center, Greenbelt, MD 20771, USA

⁵ Max-Planck-Institute for Extraterrestrial Physics, P.O. Box 1603, 85740 Garching, Germany

⁶ Raytheon ITSS, 4400 Forbes Blvd., Lanham, MD 20706, USA

Received 11 January 2000 / Accepted 11 May 2000

Abstract. Using spaceborne particle and gamma-ray detection and radio diagnostics we study solar energetic particle (SEP) production in the 1996 July 9 event. This event is associated with an impulsive soft X-ray flare (9:10 UT) and a coronal mass ejection (CME). In a global classification the event is considered as mixed-impulsive. A sequence of acceleration processes is identified, starting early in the flare impulsive phase and continuing throughout the period when the CME propagated up to several R_{\odot} above the photosphere: (1) Gamma-ray, hard X-ray and cm-wave emitting particles seen during the flare impulsive phase in the low corona had no counterpart at the Solar and Heliospheric Observatory (SoHO) spacecraft. (2) Electrons accelerated at a coronal shock wave were revealed by decimetric-to-metric type II radio emission and by simultaneous radio signatures of beams traveling to 1 AU. (3) Mildly relativistic (≥ 250 keV) electrons detected by SoHO did not correspond to these shock-accelerated populations, but to later mainly impulsive injection which was associated with radio brightenings over a large range of coronal altitudes. (4) Energetic protons detected by SoHO were accelerated during about 100 min after the flare impulsive phase with a gradually evolving production profile that bore some similarity with the time profile of broadband metric (type IV) emission. (5) While all other particle signatures decayed, a second period of interplanetary proton production took place ≥ 2 hours after flare onset. The first, 100 min period of SEP acceleration, post-impulsive phase coronal acceleration, is definitely dominant in mildly relativistic electrons. Two acceleration periods nearly equally contribute to the production of ~ 20 MeV protons. However, the second period is more productive in low energy, ~ 1 MeV, protons.

The timing of the SEP injections indicates that neither the impulsive flare acceleration in the low corona nor the interplanetary CME at $\geq 10 R_{\odot}$ are the main sources of the high-energy particles observed onboard SoHO. We suggest that various acceleration processes related to the reconfiguration of the corona in the course of the flare and CME lift-off contribute to the in-

teracting and escaping particle populations, with different signatures at different energies and in different species.

Key words: Sun: corona – Sun: flares – Sun: particle emission

1. Introduction

There are a variety of acceleration processes that may produce suprathermal, energetic and relativistic particles in the solar corona and the solar wind. They include acceleration by direct electric fields, waves, and shock waves. Miller et al. (1997) discuss the performance of each of these candidate accelerators in the context of solar flares. Shock waves driven by fast coronal mass ejections (CMEs) are considered as an independent accelerator in the corona and interplanetary space (Reames 1999 and references therein).

Observational constraints are provided on the one hand by remote sensing observations of particles interacting in the solar atmosphere, whereupon they emit at γ -ray, hard X-ray (HXR) and radio wavelengths. With the exception of nuclear γ -ray lines and neutrons (the latter are detectable in the most energetic events), these diagnostics probe electrons. Direct measurements of electrons and ions have been made aboard satellites at heliocentric distances greater than 0.3 AU. Ideally one would like to combine the different diagnostics to infer where, when and how the particles were accelerated. However, transport and probably re-acceleration modify the particle populations on their way to the detector, so that the populations measured *in situ* may be of different origin than the interacting particles. A scenario of this kind is the proposed acceleration of large solar energetic particle (SEP) events by the bow shocks of CMEs at heliocentric distances above 5–15 R_{\odot} (Kahler 1994), where it is presumed that particles accelerated in the magnetically stressed corona in association with flares play a negligible role.

Few observational tests are at hand which might allow to probe the connection of SEPs with coronal acceleration sources. Similarities in the temporal evolution of hard X-rays, radio

waves and particle fluxes measured close to the Sun (Bieber et al. 1980; Kallenrode & Wibberenz 1991; Akimov et al. 1996; Klein et al. 1999) suggest that such relationships do exist, but the quantitative correlation e.g. between the fluxes of protons interacting in the corona and those detected at 1 AU during given events is loose (Ramaty et al. 1993; Cliver et al. 1989). The particle signatures at 1 AU clearly depend on a range of processes on active region scales and on global scales, including acceleration in flare related small-scale structures as well as in widespread regions associated with a chromospheric or coronal “Moreton” wave (Kocharov et al. 1994; Torsti et al. 1998, 1999; Krucker et al. 1999) or a CME (e.g., Maia et al. 1999; Klein et al. 1999).

The acceleration and propagation of particles in the middle and high corona are difficult to probe by remote sensing techniques, since collisional radiation processes are inefficient due to the low target density. However, suprathermal electrons generate collective radio emission at frequencies from a few GHz to about 1 MHz, which is sensitive to the accelerated electrons as well as to the ambient medium from the low to the high corona. In the present paper we analyze the particle signatures related to a flare and CME on 1996 July 9. This SEP event was observed under particularly quiet conditions of interplanetary transport (Torsti et al. 1997; Kocharov et al. 1997), so that uncertainties introduced by the transport are minimal. We employ measurements of energetic protons and mildly relativistic electrons, respectively by the Energetic and Relativistic Nuclei and Electron (ERNE) instrument and the Comprehensive Suprathermal and Energetic Particle Analyser (COSTEP) aboard the SoHO spacecraft. Coronal electron acceleration and propagation is probed by radio observations using spectrography from ground (radio spectrographs at Bern, Hiraiso and Tremsdorf) and space (the WAVES experiment aboard Wind) and imaging observations (Nançay Radioheliograph). Sect. 2 of this paper presents the particle data and the derived injection functions. Sect. 3 describes the radio observations and identifies potential sites of coronal acceleration. These are compared with the inferred particle injections in Sect. 4.

2. Solar energetic particles

The 1996 July 9, 9:10 UT flare occurred in the NOAA region 7978 on the western hemisphere of the Sun, S10° W30°, about 30° eastward of the nominal interplanetary magnetic flux tube connected to the SoHO spacecraft (solar wind speed was $\approx 400 \text{ km s}^{-1}$ according to SWE/Wind observations). Gamma-ray signatures of energetic ions and relativistic electrons at the Sun were recorded with the Compton Telescope instrument (Schönfelder et al. 1993) aboard the Compton Gamma-Ray Observatory spacecraft (COMPTEL/CGRO).

2.1. Gamma-ray observation of the flare impulsive phase

Observations at HXR/ γ -ray energies of the 1996 July 9 flare event could be obtained by COMPTEL/CGRO until about 9:16 UT when CGRO entered orbital night. The COMPTEL instru-

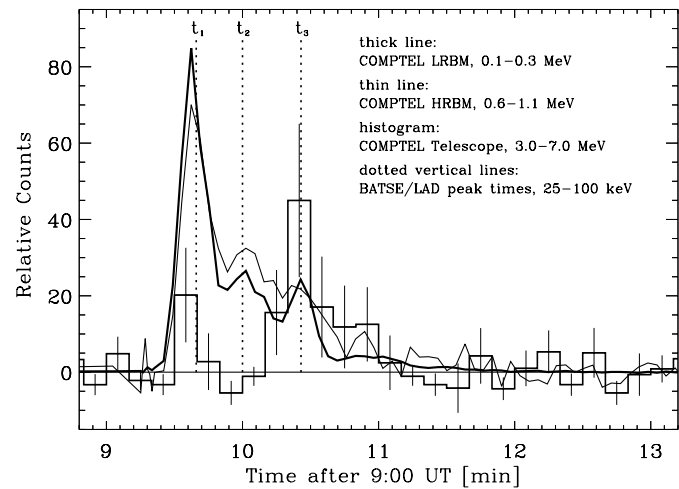


Fig. 1. Observations of the impulsive phase of the 1996 July 9 flare event with COMPTEL/CGRO. The plotted data are corrected for detector life time effects, background is subtracted, and the data sets have been scaled relative to each other. The different energy channels have been obtained with COMPTEL’s two burst detectors, high and low range burst module (HRBM and LRBM, respectively), and with the Compton telescope configuration. The peak times measured by the BATSE large area detectors are also indicated.

ment measured a signal in the Compton-telescope configuration which is sensitive to γ -ray photons of 0.75–30 MeV, as well as in the two single burst detectors which detect photons in the energy range 100–600 keV and 600–11000 keV, respectively. Fig. 1 gives the measured time profiles and allows to compare the timing of different energy ranges.

Both burst detectors register the maximum of the emission at about 9:09:40 UT followed by two smaller emission peaks. The times agree very well with the peak times measured by the BATSE large area detectors for energies 25–100 keV (denoted t_1 , t_2 , and t_3 in Fig. 1). All three emission curves originate from bremsstrahlung of electrons with an energy in the range of roughly 50 to a few 100 keV.

The signal in the 3–7 MeV channel originates from nuclear line emission which is emitted when protons and/or ions with an energy of about 10–20 MeV/nucleon interact with ambient material in the chromosphere. As can be seen in Fig. 1 the main emission in this energy range coincides with the third peak at t_3 of the electronic emission. A faint signal can be seen also for the first peak at t_1 , but no significant emission is seen during the second peak at t_2 . A signal of the 2.2 MeV line was detected well before t_3 . The emission in the 2.2 MeV neutron capture line is produced with a time delay of about one minute and requires reactions of protons and/or ions with an energy in the range of about 10–100 MeV/nucleon. The detection of this signal confirms that the emission during the first peak stems indeed from nuclear lines, and that protons and/or ions accelerated up to energies of at least 10 MeV have to be present.

It is known that the ratio of accelerated electrons to protons can vary from flare to flare, or within flares (e.g., Chupp et al. 1993; Marschhäuser et al. 1994; Miller et al. 1997). Here, the

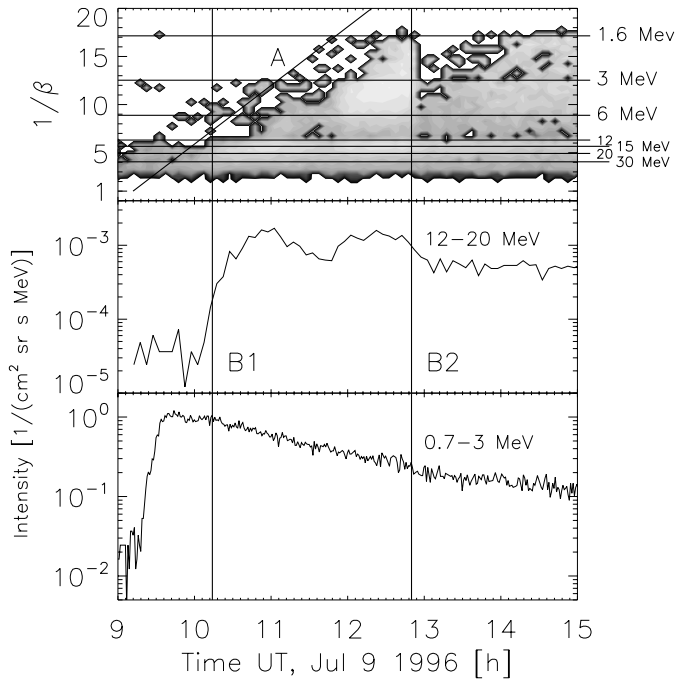


Fig. 2. Proton arrival time vs. $1/\beta \equiv c/V$ scatter plot visualized in a gray scale proportional to the product of the V^6 times intensity, V being proton velocity (upper panel); also the intensity-time profiles of 12–20 MeV protons (middle panel) and 0.7–3 MeV electrons (lower panel). The tilted line *A* illustrates expected arrival times of first protons if injected from the Sun at 9:12 UT – 500 s.

ratio is highly variable for the three observed peaks: the emission at t_1 and t_3 includes nucleonic signatures, while during the peak at t_2 it appears to be dominated by the electron bremsstrahlung.

From the perspective of the particle injection times the COMPTEL measurements show that the main HXR emission caused by ~ 100 keV electrons occurred at 9:09:40 UT, while the main γ -ray line emission caused by >10 MeV protons appeared somewhat later at 9:10:20 UT. However, high-energetic protons are present from the beginning of the event.

2.2. Overview of the SEP event

The solar energetic particle event was observed with the energetic particle detectors ERNE (Torsti et al. 1995) and COSTEP (Müller-Mellin et al. 1995) aboard SoHO. The interplanetary proton event was weak enough for ERNE to be able to record nearly every individual particle as pulse height data. For the goals of present analysis, the ERNE recorded protons have been divided into six energy channels: 1.6–3 MeV, 3–6 MeV, 6–12 MeV, 12–15 MeV, 15–20 MeV and 20–30 MeV. The lowest channel has a geometrical factor of $0.260 \text{ cm}^2 \text{ sr}$ and the next two $0.915 \text{ cm}^2 \text{ sr}$, thus the statistics are lower on these channels compared to the three highest energy channels possessing geometric factors of $\sim 30 \text{ cm}^2 \text{ sr}$.

The time versus inverse-velocity scatter plot is shown in the top panel of Fig. 2. The horizontal lines mark the energy channel limits. Velocity dispersion is seen in the beginning of the event

indicating arrival of particles from the Sun. The observed solar wind velocity of nearly 400 km s^{-1} implies the interplanetary magnetic line length of $\approx 1.2 \text{ AU}$. The oblique line *A* in the figure corresponds to this distance traveled from the reference time 9:12 UT – 500 s, the soft X-ray maximum time. We have attempted to estimate first injection time and the distance traveled also from our proton data using a kind of velocity-dispersion technique described by Torsti et al. (1999). However, in 3–12 MeV channels there was also contribution of the previous flare observed on the same day at 7:58 UT (SGD 1996). This adds uncertainty to the estimation. With data in hand we can rule out injection of first protons before 9:08 UT – 500 s and after 9:28 UT – 500 s (with a view to comparison with results of radio observations, we artificially add to and then explicitly subtract from the particle injection time the 500 s value required for radio waves to travel from near-Sun to Earth). Thus based on velocity dispersion, we can estimate the first proton injection time as $t_{P1} = (9:18 \text{ UT} - 500 \text{ s}) \pm 10 \text{ min}$.

Fig. 2 also illustrates an abrupt decrease of proton flux, simultaneously seen in all energy channels at 12:50 UT. This fall of intensity indicates entering a new magnetic flux tube with very different proton transport conditions (Kocharov et al. 1997). The tube named a slow transport channel (STC) had been traversed at 16:00 UT on July 9, 1996. In our present study, we do not consider observations after entering STC. The employed period is limited by vertical lines *B1* and *B2* in Fig. 2.

On the middle panel of Fig. 2 we present the 5-minute averaged proton intensity in the energy channel of 12–20 MeV employed for the anisotropy measurement. In order to gain better statistics, the channel is wider than in the anisotropy study by Torsti et al. (1997), but otherwise the method is similar. A high anisotropy observed during the entire event (excluding STC) implies a prolonged injection of protons at the Sun. There were two peaks in the injection. The first peak of the 12–20 MeV proton flux was about 90 min long, while only a portion of the second peak was observed before entering a new flux tube at 12:50 UT.

Relativistic electron flux was recorded with the COSTEP instrument (Bothmer et al. 1997). The electron event start corresponds to the injection of first electrons several minutes after the soft X-ray emission maximum, 9:12 UT – 500 s (cf. vertical line *A* in Fig. 3). Two sub-peaks can be seen at the top of the 0.25–0.7 MeV electron profile (Fig. 3), but dip between them is rather shallow. Entering a new transport channel (STC), observed with protons at 12:50 UT, is only marginally observable in the electron profile (marked with line *B* in Fig. 3). The STC effect in electrons is much weaker than in protons.

2.3. Scenario of electron injection

The electron intensity maximum (Fig. 3) is too flat and decays too fast to be fitted with an exactly impulsive injection, but the introduction of minor additions before and after the main injection pulse produces a satisfactory fit. We have fitted the SoHO-observed electron event with three impulsive injections, using the injection time and injection strength as free param-

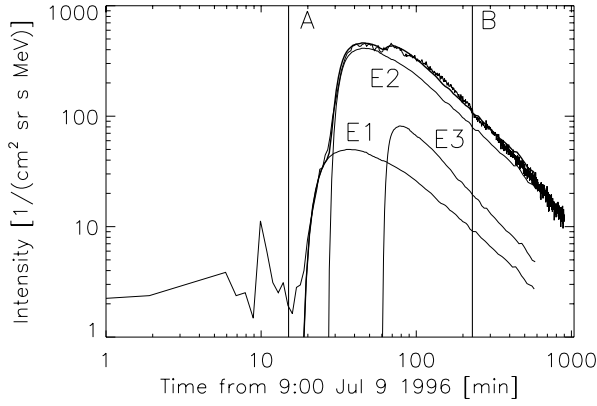


Fig. 3. The 0.25–0.7 MeV electron intensity as observed by the COSTEP/SoHO instrument (fluctuating curve) and the theoretical intensity (unlabeled heavy solid curve) comprising the main impulsive injection E2 and two minor injections E1 and E3 (correspondingly labeled light solid curves). Expected arrival of first electrons injected from the Sun at 9:12 UT – 500 s is shown with vertical line A. Start of the new magnetic flux tube (STC) is shown with line B. A spike at 9:10 UT is caused by the flare hard X-ray pulse.

eters. The transport model parameters have been adopted as explained in Appendix. The best-fit curve in the case of the three-pulse injection is shown in Fig. 3. It fits well the observed intensity-time profile. The deduced injection times at the Sun are $t_{E1} = 9:17 \text{ UT} - 500 \text{ s}$ (the first minor pulse of injection), $t_{E2} = 9:26 \text{ UT} - 500 \text{ s}$ (the major injection peak) and $t_{E3} = 9:58 \text{ UT} - 500 \text{ s}$ (the last minor peak). Contribution of the injections to the total 0.25–0.70 MeV fluence is 9%, 76% and 15% for the E1, E2 and E3 pulses, respectively. Note that the decay of the first minor injection, E1, and also the rise of the last minor injection, E3, were essentially overlaid by the major peak, E2. For this reason, time profiles of the minor injections could not be precisely deduced, but t_{E1} should be regarded as the first electron injection time, while t_{E3} gives a $\pm 5 \text{ min}$ estimate of the last injection time. Uncertainties in the determination of t_{E1} and t_{E2} do not exceed $\pm 2 \text{ min}$. Thus, the major electron injection is impulsive and occurs not earlier than 15 min after the flare start.

An analysis of the pulse-height data for the period 9:18–10:18 UT within the 0.25–1.5 MeV energy range indicates nearly power law differential energy spectrum: $I(E) \sim E^{-4.3}$ (H. Sierks, pers. comm. 1999). The total number of $> 0.25 \text{ MeV}$ electrons injected at the Sun is $N_e(> 0.25 \text{ MeV}) = 4 \times 10^{32}$ per sr of the heliocentric solid angle (i.e. per the R_{\odot}^2 area of solar surface at the root of the Earth-connected interplanetary magnetic field line).

The mildly relativistic electrons seen by COSTEP are associated with an electron event observable also at lower energies, from about 1 keV to hundreds of keV, as detected by the 3-D Plasma and Energetic Particle experiment on the Wind spacecraft (Lin et al. 1995). Determining the solar release time from the energy dispersion of the electrons at the spacecraft (Krucker et al. 1999), S. Krucker (pers. comm. 1999) finds that the first electrons are released at the Sun at $(9:21 \text{ UT} - 500 \text{ s}) \pm 3 \text{ min}$.

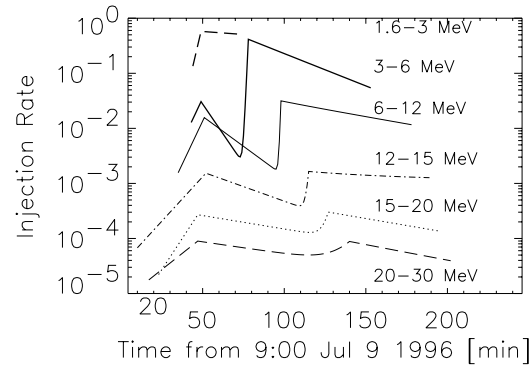


Fig. 4. Solar injection rate profiles for protons. The injection rate is shown in units 1.5×10^{29} protons / (min MeV) per solar hemisphere; time as it was at the Sun. A *d*-component contribution to the 1.6–3 MeV channel has not been calculated.

We have deduced with the COSTEP data the first injection time $t_{E1} = (9:17 \text{ UT} - 500 \text{ s}) \pm 2 \text{ min}$. Given the different techniques of analysis, the onset times of the electrons at Wind and of the mildly relativistic electrons at SoHO are consistent. A mean estimate for the first electron injection time finally is $(9:18\text{--}9:19) \text{ UT} - 500 \text{ s}$. That implies that the electron injection into interplanetary space occurs nearly ten minutes after the onset of the radiative signatures of the flare.

2.4. Scenario of proton injection

Proton injection functions are deduced by a careful fitting of the observed anisotropy and intensity-time profiles. A choice of proton transport model is described in the Appendix. Several injection scenarios have been studied. In particular, we attempted to fit the proton intensity-time profile with an injection scenario deduced for relativistic electrons, but it became evident that the proton injection is prolonged and the impulsive injection scenario is not applicable. Several other scenarios were also tested before we decided to use a double-exponential injection profile (the alternative scenarios are described more thoroughly in Sect. 4.2.3). The injection rate is finally approximated in the following form

$$q(t, E) = q_1(t, E) + q_2(t, E), \quad (1)$$

where

$$q_i(t, E) = A_i \exp[\Phi_i(t)], \quad (2)$$

$$\Phi_i(t) = D_i(t - t_i^{\max}) \quad \text{at } 0 < t \leq t_i^{\max}, \quad (3)$$

$$\Phi_i(t) = -(t - t_i^{\max})/\tau_i \quad \text{at } t > t_i^{\max}. \quad (4)$$

The fitting parameters, D_i , τ_i and t_i^{\max} , dominate the injection rise, decay and the maximum injection time, respectively (Fig. 4). Those parameters were allowed to be energy dependent and adjusted to get a best fit for each energy channel. The normalization factors A_i determine injection energy spectra for the first and second injection components, $i = 1, 2$. Similar to the 1990 May 24 event study (Torsti et al. 1996), we call the 1st and 2nd injections *p*-component and *d*-component injections, respectively.

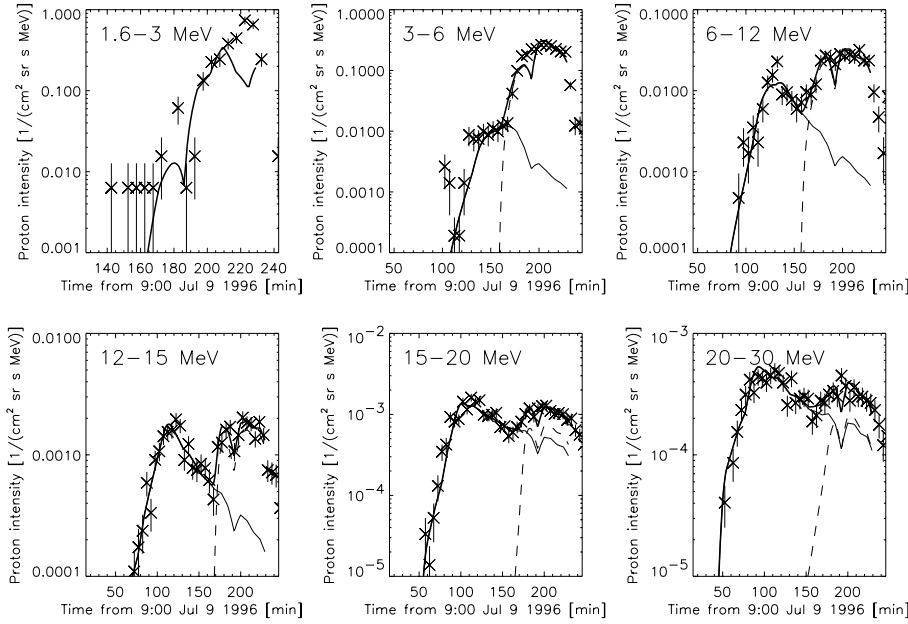


Fig. 5. Theoretical (curves) and observed (asterisks) proton intensities in six energy channels. The double-exponential injection model has been used (see Eqs. 1–4 and Fig. 4). Light solid and dashed curves are for p- and d- components of injection, respectively. Heavy solid curves are for sums of the components.

SoHO is a three-axis stabilized spacecraft and thus ERNE’s particle detectors do not cover the whole 4π solid angle, and the magnetic field direction is not stable. In order to take this into account we calculate the differential acceptance of the detector as a function of time and pitch angle and convolve it with the interplanetary transport function to get a value of the proton intensity averaged over the instrument acceptance cone. The resulting intensity curve is directly comparable with the experimental intensities (Fig. 5).

Highest uncertainties are expected in the low energy channels, 1.6–3 MeV and 3–6 MeV. In the lowest energy channel the instrument consists of two detectors with a narrow, 32° , field of view. This results in a high sensitivity to the magnetic field direction, if proton anisotropy is large. In addition, low energy protons arrived too close to the slow transport channel. Also the influence of the earlier flare contaminates the 3–6 MeV channel (Fig. 2). In this view, we had decided for the two lowest energy channels not to vary the maximum injection time, t_1^{\max} , but to set it equal to the time obtained from the four higher energy channels. Furthermore in the lowest, 1.6–3 MeV, channel, we do not attempt to fit the d-component portion of the intensity profile, i.e. the last 3–4 points in the upper left frame of Fig. 5. Those data points certainly indicate a new rise, but uncertainties of fitting few points would be very large.

The deduced injection functions are presented in Fig. 4. In this figure, we do not show initial portions of injection profiles before the maximum cumulative effect of the injection exceeds the 3σ level above background. The portion of injection curves from which the particles would not reach SoHO before entering the new magnetic tube (STC) is also left out. It is seen from Fig. 4 that the maximum injection of the p-component protons occurred around 9:50 UT (the corresponding near Earth light-arrival time is $t_1^{\max} + 500 \text{ s} \approx 9:58 \text{ UT}$). No energy dependent trend in the maximum injection time, t_1^{\max} , is seen. The variance of t_1^{\max} illustrates statistical uncertainties, $\pm 2.5 \text{ min}$. It is

noteworthy that the maximum time of the p-component proton injection, t_1^{\max} , is close to the deduced time of the last electron injection, t_{E3} . On the other hand, the earliest observable injection of protons occurred close to the time of the first electron injection t_{E1} (see the 12–15 MeV proton injection profile in Fig. 4). The first and the last electron injection times, t_{E1} and t_{E3} , bracket the rise phase of the p-component proton production. Those minor electron injections might be related to protons, and a kind of continual minor production of electrons between t_{E1} and t_{E3} cannot be ruled out.

Amplitudes A_1 and A_2 (Eqs. 1, 2) give the proton injection spectra at the peak injection time for the p-component and the d-component, respectively. Best power law fits to the deduced differential energy spectra are obtained for the spectral indexes $S_1 = 3.6$ and $S_2 = 5.5$. Total numbers of the p- and d- component protons injected at the Sun are respectively $N_1(> 10 \text{ MeV}) \approx 2 \times 10^{28}$ and $N_2(> 10 \text{ MeV}) \approx 4 \times 10^{28}$ per sr of the heliocentric solid angle. Note that the d-component is dominant at low energies and correspondingly in the total proton energetics.

3. Radio observations as tracers of coronal electron acceleration

3.1. Spectrographic observations

During the 1996 July 9 event enhanced levels of radio emission were observed from 15 GHz in the low corona to some tens of kHz at 1AU. Different aspects of the radio emission during the first minutes of the event were discussed by Mann et al. (1997), Dryer et al. (1998), Karlický (1998), Pick et al. (1998) and Klassen et al. (1999). Fig. 6 shows whole Sun observations between the event onset and 10:30 UT, covering the time interval of the identified electron injections and of most of the p-component proton injection. The times of the impulsive

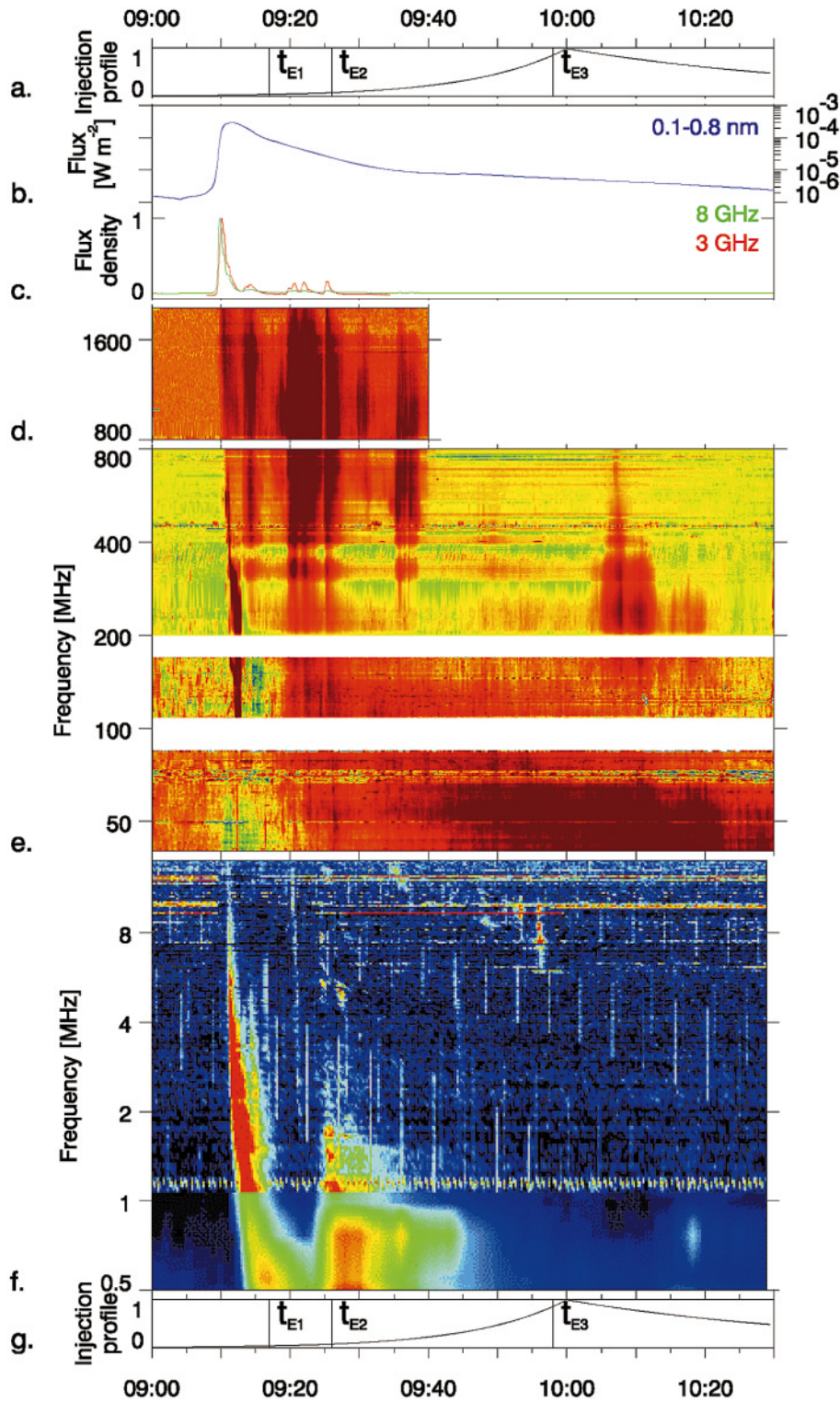


Fig. 6a–g. Comparison of the particle injection functions with remote sensing observations of the radio and soft X-ray emission. **a, g:** Times of the mildly relativistic electron injections (vertical lines) and time profile of the p-component proton injection (curve). Solar injection times are shifted by +500 s for comparison with radio and X-ray data. **b:** Time history of the soft X-ray flux (GOES, 0.1–0.8 nm). **c:** Time history of microwaves at 8 GHz (green; Berne) and 3 GHz (red; Ondřejov). **d–f:** Dynamic spectrograms at decimetric (**d**; Hiraíso Observatory), decimetric-decametric (**e**; Potsdam-Tremsdorf Observatory) and hectometric waves (**f**; the WAVES experiment aboard Wind). High brightness is red, background is green/yellow (**d, e**) or blue (**f**). The early bright emission in the range 40–90 MHz is a noise storm which fades at the onset of the event under discussion.

injections of mildly relativistic electrons and the evolution of the p-component injection of protons in the 12–20 MeV energy channel are plotted at the top and bottom of the figure.

The GOES soft X-ray time profile (0.1–0.8 nm; Fig. 6b) shows a rapid rise from a perturbed pre-event background to maximum followed by a decay in three steps with successively longer decay times: 9:11:30 UT (peak time) – 9:17 UT, 9:17 –

9:40 UT, 9:40 UT until about 11:30 UT. The narrow major peak suggests that the event belongs to the class of impulsive soft X-ray flares. However, the complex behavior during the decay of the event probably reveals different episodes of energy release on increasing temporal and spatial scales.

We are going to describe separately the three spectral ranges of radio emission in the following.

3.1.1. Microwaves (8 GHz, 3 GHz)

Microwave radiation (Fig. 6c) is emitted by mildly relativistic electrons (typically 100 keV to a few hundreds of keV) interacting in the low corona (below $\approx 0.1 R_{\odot}$ above the photosphere). The time profiles in Fig. 6c show a strong impulsive peak similar to the hard X-rays and γ -rays (cf. Fig. 1). The impulsive microwave peak has a spectral maximum near 9 GHz (SGD 1996). It is followed by a series of weaker enhancements, which are less pronounced at 8 GHz than at 3 GHz and extend well into the meter wave range.

3.1.2. Decimetric to decametric emission (2000–40 MHz)

The emissions in this range (Fig. 6d,e) are produced by suprathermal electrons (poorly known energy range, presumably a few tens to a few hundreds of keV) at coronal heights between roughly a few 10^4 km and $1 R_{\odot}$ (middle corona; the typical source height increases with decreasing frequency). The plotted spectra are obtained after the elimination of frequency channels disturbed by terrestrial transmitters and subtraction of a pre-event spectrum. The initial bright feature between 600 and 100 MHz (9:11–9:13 UT) is a type II burst, due to electrons accelerated at a shock wave. A faint decametric type III group appears at its low frequency end (90–40 MHz, 9:11:30–9:12:30). A series of short broadband enhancements, the counterparts of the late microwave enhancements (Fig. 6c), are seen between 9:13:20 and 9:39 UT. Initially, they appear in the decimetric waves (2000–300 MHz), but the later emissions extend across the entire decimeter-to-decameter wave range. They are associated with a diffuse continuum emission, which is best visible in the spectrogram below 200 MHz, but which also extends to higher frequencies. The low frequency limit of the continuum emission drifts gradually to lower frequencies. The continuum fades a few tens of minutes after the last broadband enhancement. It is no longer seen on the spectrographic records after ~ 11 UT.

The short broadband enhancements display little spectral fine structure. Detailed inspection of the brightening near 9:25 UT in the data of the Trensdorf Spectrograph and the Nançay Radio Heliograph shows a smoothly evolving emission with only few superposed bursts, the most prominent one being a type III burst between 500 and 600 MHz near 9:25:10 UT. A few faint decametric type III bursts are observed before and afterwards. In the decimeter range the peak brightness temperatures measured with the NRH during the enhancement near 9:25 UT rise from $\sim 3 \times 10^8$ K at 237 MHz to $\sim 8 \times 10^8$ K at 432 MHz, which is consistent with the increasing flux density from low to high frequencies displayed by the dynamic spectrum in this range (Fig. 6e). The spectral shape and the brightness temperatures are consistent with optically thick gyrosynchrotron radiation at decimetric waves, whereas the 3 and 8 GHz fluxes point to optically thin gyrosynchrotron emission. Hence, we suggest that the broadband brightenings are emitted by mildly relativistic electrons in the corona. These enhancements occur during the second part of the soft X-ray decay, which has a longer time

constant than the preceding decrease. The last broadband enhancement at about 9:35 UT occurs near the instant when the decaying soft X-ray profile flattens for the second time. It has no counterpart at 8 GHz, suggesting that the electrons radiate in weaker magnetic fields than precedingly.

3.1.3. Hectometer emission (<14 MHz)

Radio emission in the range 14–1 MHz (Fig. 6f) is typically emitted between 1 and $20 R_{\odot}$ above the photosphere. The most prominent features are two groups of type III bursts, at 9:11 and 9:24 UT, generated by electron beams traveling from the corona into interplanetary space (energies of a few keV to a few tens of keV). Both type III groups have several components, as seen near their high frequency end and both groups are observed below 1 MHz down to the plasma frequency at the satellite level. The first group, starting at 9:10:57 UT, which is well defined in the entire frequency range below 14 MHz, starts well after the impulsive microwave burst at 9:09:05 UT and therefore appears not to be produced by electrons accelerated in the low corona. Rather, this type III group occurs simultaneously with the decimetric-metric type II burst associated with the shock wave in the middle corona, and with the decametric type III bursts at 9:12 UT. However, this first type III group does have a very weak secondary component at 9:14 UT that becomes visible at frequencies below 5 MHz and which occurs 1 minute after the end time of the metric type II. This weak component also occurs 1 minute after the first weak microwave enhancement and could be related to it.

The second hectometric type III burst has only faint, but nonetheless significant, traces between 14 and 2 MHz. It occurs at about the same time as the broadband cm-m-wave enhancement around 9:25. The frequency drift seems to be faster than during the first type III burst, but it is hard to determine accurately due to the intermittent spectrum at high frequencies and the superposition of both type III bursts at and below 1 MHz.

Between 9:30 and 10 UT a highly intermittent and weak signature of a type II burst is seen between 14 and 6 MHz.

3.2. Source configuration at decimeter and meter waves

Imaging observations were carried out at five wavelengths in the decimetric and metric range by the Nançay Radio Heliograph (henceforth NRH; Kerdran & Delouis 1997). In the following the evolution of the radio sources is briefly presented in order to demonstrate that magnetic restructuring and electron acceleration continue in and around the active region during several hours after flare onset.

Fig. 7 shows snapshot maps at several frequencies. A noise storm existed above the active region before flare onset (first row). It reveals long lasting electron acceleration which is unrelated to the flare under discussion. The subsequent type II and continuum emission during the first hour of the event have been discussed in detail by Pick et al. (1998). The second row of Fig. 7 (9:14:30 UT) displays sources at 410 and 237 MHz during one of the broadband enhancements.

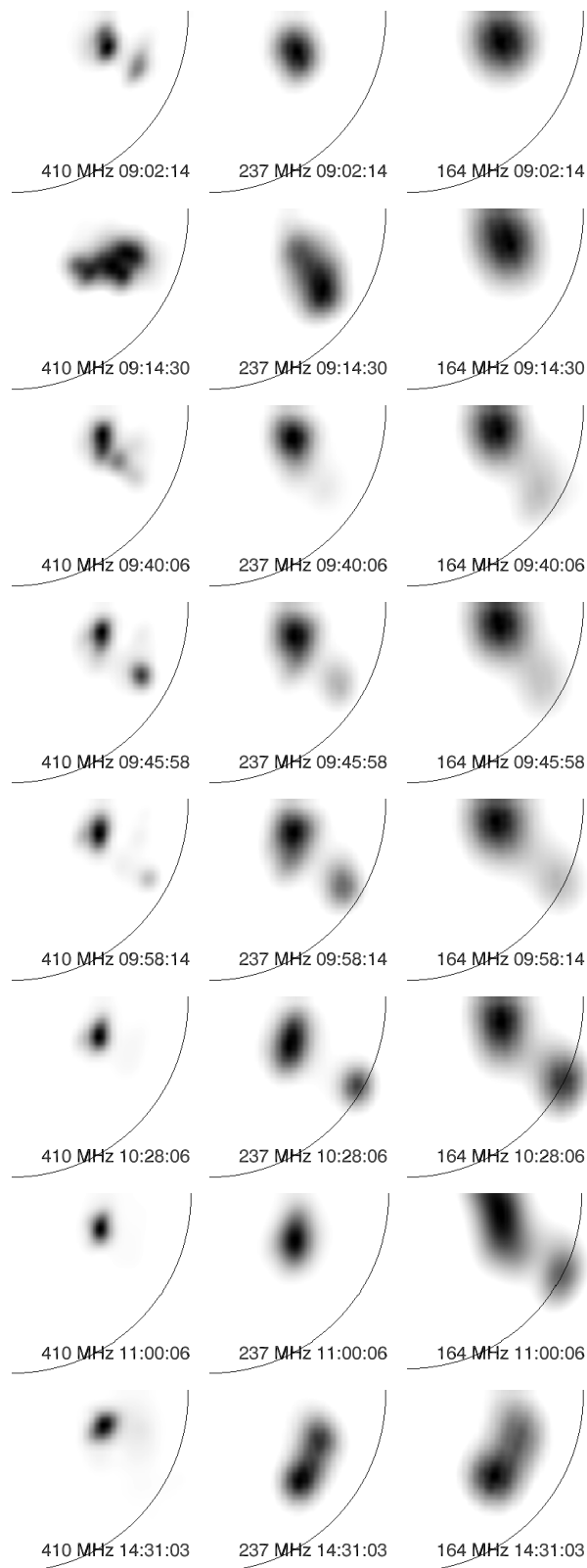


Fig. 7. Snapshot maps at three frequencies during the late evolution of the 1996 July 9 event (Nançay Radio Heliograph). Each row corresponds to a given time, each column to a given frequency. Integration time is 32 s in the first seven rows, 128 s in the last row. Only intensity values above the average of each map are plotted. Brightness increases linearly from white to black. The quarter circle traces the optical limb.

After 9:40 UT the source configuration evolves in a similar way at all frequencies observed by the NRH. The emission fades progressively at successively lower frequencies, but structural changes continue during several hours at the lowest observed frequencies, suggesting that the main sites of electron acceleration rise gradually from the low to the middle corona:

- After 9:40 UT a discrete source is seen to brighten to the south-west of the continuum emission. It drifts away from the active region at a projected speed of $40\text{--}50\text{ km s}^{-1}$ at all frequencies. At 10:30 UT it has faded from view at 410 MHz, but persists as a stationary source above the south-western limb at low frequencies. It remains visible until 11:22 UT at 164 MHz. During the slow south-westward motion of this source new brightenings appear between it and the continuum source above the active region. The source motion is much slower than the speeds of $330\text{--}450\text{ km s}^{-1}$ deduced for different features of the CME (Pick et al. 1998). It reveals continued restructuring and/or magnetic field expansion in the low corona, in association with the decametric continuum emission at greater height.
- The meter wave source above the active region does not recover its pre-event shape after fading of the moving source. Even more than five hours after flare onset the 237 and 164 MHz maps show ongoing structural changes (Fig. 7, last row) with alternating brightenings of two or more sources in a large north-south oriented complex. The source complex extends below the brightest part of the CME (Pick et al. 1998, Fig. 4).

4. SEP injection and its relationship with coronal processes

The remote sensing data show different signatures of rapidly and slowly evolving energetic particle populations in the corona: γ -ray, hard X-ray and centimetric radio emission from the initial impulsive acceleration of electrons and protons in the low atmosphere, long lasting acceleration of the electrons emitting the broadband continuum, repeated episodes of impulsive acceleration in the corona leading to the broadband enhancements, and shock acceleration of electrons in two different altitude ranges producing type II emission. Continued changes in the structure of metric radio sources show the persistence of electron acceleration until at least five hours after the start of the flare. Both impulsive and long lasting processes of particle acceleration were independently inferred for the electrons and protons of the SEP event. We now discuss the possible relationship between the coronal processes and the particle populations seen at 1 AU, referring especially to Fig. 6.

4.1. Impulsive phase acceleration

We identify the impulsive phase with the first minutes of the event (9:09–9:11 UT), when bright microwave and moderately intense hard X-ray and γ -ray emissions are observed. Although no γ -ray and hard X-ray data are available after 9:16 UT, because CGRO is in the Earth's shadow, the microwave profile and the continuous decrease of the soft X-ray flux suggest that

the impulsive phase is finished at that time. From the absence of emission at metric and decametric wavelengths during the impulsive phase we conclude that the accelerated particles are initially injected into closed magnetic structures of the low atmosphere. This would also explain why no signature of the mildly relativistic electrons and the energetic protons accelerated during the impulsive phase is observed at 1 AU, although the flare occurs close to the nominal Earth-connected magnetic field line. The subsequent drift of the low-frequency limit of the radio emission towards lower frequencies shows that particles (at least electrons) have successively access to more dilute plasmas, i.e. higher coronal altitudes. The association with a CME probably means that the low lying magnetic structures are gradually opened and expand.

Similar events where no interplanetary counterpart of impulsive phase acceleration was detected, although the satellite was nearly well connected to the flare site, were reported in the literature. For instance, during the large SEP events on 1990 May 24 at W76° (Torsti et al. 1996; Debrunner et al. 1997, Kocharov et al. 1999a) and 1991 June 15 at W69° (Kocharov et al. 1994; Akimov et al. 1996) the comparison of γ -ray and neutron observations with particle measurements in space showed that protons started to be injected into flux tubes connected with the satellite ~ 10 minutes after interacting protons with comparable energies were detected in the low solar atmosphere. The radio spectrum of the 1991 June 15 event has a similar drift towards lower frequencies as 1996 July 9 (Akimov et al. 1996). No dynamic spectrum at meter waves is available for the 1990 May 24 event, but Lee et al. (1994) show that the microwave spectrum displays a systematic gradual drift from 10 GHz to 1 GHz within ~ 3 min. However, many impulsive flares with prominent hard X-ray and γ -ray emission do not display such delays (Raoult et al. 1985), and interplanetary electrons were observed to be injected during the impulsive phase of solar flares (Bieber et al. 1980; Kallenrode & Wibberenz 1991). We surmise that the access of particles from coronal acceleration sites to interplanetary space is different in different events. This could be ascribed to different configurations and evolutions of the magnetic field in the vicinity of the acceleration site(s). A key role of a CME is that it will open magnetic fields (cf. also Manoharan et al. 1996). The CME is then an essential ingredient of the energetic particle event, irrespective of whether it contributes to the acceleration or not.

4.2. Post-impulsive acceleration

4.2.1. Shock acceleration in the middle corona

The type II burst emission at decimetric-to-hectometric wavelengths is evidence for electron acceleration at shock waves in the middle and high corona. If the shock speed derived from meter wave observations is ≥ 1000 km s⁻¹ (Klassen et al. 1999), a single large-scale shock cannot generate the type II bursts in the two frequency ranges. The hectometric type II burst suggests a velocity ≤ 600 km s⁻¹. This is comparable to the CME leading-edge velocity, ~ 400 – 450 km s⁻¹, observed at a later

time when the leading-edge was already at $> 10 R_{\odot}$ (Pick et al. 1998, Fig. 8). The hectometric type II emission is probably associated with the CME when it was between 1 and $2 R_{\odot}$ above the photosphere.

The time coincidence of the first hectometric-to-kilometric type III burst and the decimetric-metric type II signature of a coronal shock strongly suggests that at least the electron beams that generate the initial part of the hectometric burst are accelerated at the coronal shock wave, especially since no simultaneous decimetric type III emission is seen in the low corona. Escape of electron beams from the shock front is also directly indicated by the observed decametric type III bursts. This and a possible acceleration mechanism were discussed by Mann et al. (1997) for the 1996 July 9 event, while Bougeret et al. (1998) presented similar evidence for a different event. On 1996 July 9 the electron beams producing the first hectometric type III burst group are accelerated about 6 minutes before the first identified injection of mildly relativistic electrons measured by COSTEP (t_{E1}) and also before the injection of suprathermal electrons detected onboard Wind.

Instead of inferring t_{E1} from the particle data and comparing it with the radio timing, we can use the radio time profile at frequencies where the type II burst is observed and compute the expected time evolution of the electrons at SoHO. Such a computation for the frequency of 327 MHz results in the expected rise of the electron intensities at 1 AU more than 5 minutes earlier than observed. This confirms that acceleration at the shock wave in the middle corona does not contribute significantly to the mildly relativistic electrons seen by COSTEP, in disagreement with the claim of Mann et al. (1997). Similarly, no significant amount of ~ 10 MeV protons from the shock is detected.

A possible interpretation of this result is that the energy of the electrons accelerated by the shock wave producing the decimetric-metric type II burst does not exceed a few tens of keV. Electrons in this energy range may be hidden in the Wind data by a preceding event (S. Krucker, pers. comm.). The result is also consistent with the statistical study performed by Hucker et al. (1992), which indicates that the presence of a type II burst enhances the flux density of an associated hectometric type III burst without changing significantly the intensity of mildly relativistic electrons. We cannot exclude, however, that particles accelerated by the shock remained undetected because of a poor magnetic connection to Wind and SoHO.

4.2.2. Acceleration of mildly relativistic interplanetary electrons

The COSTEP electron observations were ascribed in Sect. 2 to the mainly impulsive acceleration peaking at t_{E2} . Around this time a broadband enhancement is observed from microwaves down to the low-frequency limit of the Trensford spectrograph (Fig. 6e), with evidence for the acceleration of mildly relativistic electrons. The simultaneously occurring second hectometric type III group shows electrons escaping from the corona. Therefore the processes which accelerated the radio emitting electrons

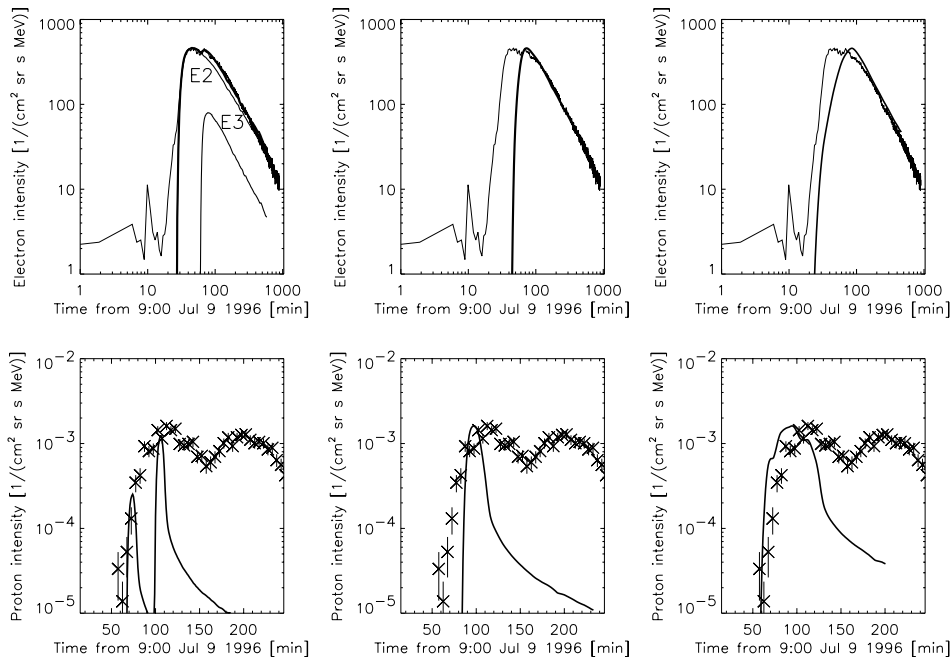


Fig. 8. Illustration of different scenarios for production of solar energetic particles: intensity–time profiles of 0.25–0.7 MeV electrons (upper row) and 15–20 MeV protons (lower row) calculated in frameworks of different injection models as compared to the experimental data. Model curves result from injection profiles **1)** in the form of two impulsive injections at $t_{E2} = 9:26\text{--}500$ s and $t_{E3} = 9:58\text{--}500$ s (left column); **2)** in the form of the intensity–time profile of the south-western radio source at 410 MHz (central column); **3)** in the form of the logarithm of the whole Sun intensity–time profile at 90 MHz (right column). The fluctuating thin curve in the upper row and asterisks in the lower row represent the experimental data. In the upper left frame, the thick curve is for the overall intensity E2 + E3; ratios of the E2 to E3 injections in the upper left and the lower left frames are different.

in the low and middle corona are the prime candidate for producing the main injection of mildly relativistic electrons into interplanetary space. The hectometric type III emission corroborates the impulsive character of the main injection of mildly relativistic electrons into interplanetary space.

Coronal shock waves of probably different origins are seen through their radio emission before and after the main injection of relativistic electrons. If one of these shocks is to be invoked as the accelerator, *ad hoc* explanation is required for the short duration of the electron acceleration to mildly relativistic energies. In the high corona, the shock is expected to accelerate more or less continuously. This is different from the middle corona, where shock acceleration can have different consequences, depending on the magnetic structures encountered (cf., e.g., scenarios proposed by Stewart & Magun 1980; Aurass et al. 1998; Bougeret et al. 1998). The temporal coincidence of the injection E2 with the broadband brightening from the low and middle corona argues in any case for acceleration behind the shock, and independent of it.

There is no decimetric-to-metric counterpart of the last minor pulse of mildly relativistic electron injection, E3. It occurs not far from the last brightening of the hectometric type II burst, but other, similar brightenings, occurred before. A more or less continual minor acceleration of electrons by the shock or another proton accelerator, starting at t_{E1} and ending at t_{E3} , cannot be excluded. An alternative is acceleration in the course of the coronal processes which give rise to the slowly drifting south-western radio source illustrated in Fig. 7. At 410 MHz, the source peaked at 9:45 UT. Using the source intensity–time profile at 410 MHz as the injection function, we find a good correspondence with the last phase of the electron event observed by COSTEP (Fig. 8, top center panel).

4.2.3. Acceleration of interplanetary protons

The proton injections have a fundamentally different character from those of the electrons. The time evolution is very slow, inconsistent with the impulsive behavior of the mildly relativistic electrons (see the left column of Fig. 8). The slow evolution of the metric–decametric continuum is similar to the p-component injection profile (cf. Fig. 6e, especially in the range 40–90 MHz). As an illustration, in the right lower panel of Fig. 8 we compute the proton intensity profile assuming that the proton injection is proportional to the logarithm of the whole Sun emission at 90 MHz. While there is not exact coincidence between the calculated and observed profiles, a similarity could be seen. The p-component of proton production is correlated with a radio continuum in the 40–90 MHz range. The corresponding height above the photosphere is $\sim 0.3\text{--}1 R_{\odot}$ (e.g., Mann et al. 1999). Thus the time evolution of the p-component proton production accompanies two signatures of coronal acceleration:

- The time extended acceleration of the electrons emitting the metric–decametric continuum at a height of $\sim 0.3\text{--}1 R_{\odot}$ above the photosphere, which is related to the large scale restructuring of the coronal magnetic field as revealed by the motion of the underlying metric radio source (Fig. 7).
- The coronal shock wave associated with the hectometric type II burst (Fig. 6f) at greater distances from the flare, about $1\text{--}2 R_{\odot}$, judging also from the height–time plot of the CME front of Pick et al. (1998).

The CME is important for the p-component proton acceleration, because it is related to both processes. However Kahler (1982) concluded from a statistical comparison of SEP associations with type II bursts and broadband continua that there is no evidence that the type II shock accelerates the protons detected in space. The type II shock signature ceases at about 10 UT.

Even if this does not prove that the shock decays in the high corona, it is in line with the measured low speed of the CME and the absence of kilometric type II emission, which Cane et al. (1987) showed to be an unambiguous signature of fast CMEs in interplanetary space. Indeed no shock signature was detected in interplanetary space despite dedicated research (Dryer et al. 1998).

The p-component injection was followed by the delayed rise of the second (d-component) proton acceleration. The d-component proton injection has no suggestive coronal counterpart. This acceleration produces a steeper spectrum and a higher particle flux at energies below ~ 6 MeV than the first acceleration. In terms of the energetics of the proton population the delayed injection is more important than the p-component injection, but it is not dominant at high energies. Although the radio and soft X-ray observations show that energy is continuously released during several hours in and around the active region, nothing indicates that the amount of energy release increases until the maximum of the delayed proton injection near 11 UT. An earlier onset of the second injection at lower energies (Fig. 4) indicates a new, slow acceleration of protons after the first production has decayed. These observations support the idea that the proton acceleration is driven by the CME. In this case the acceleration of the delayed proton component would be maximum at projected heights of about $4 R_{\odot}$ (cf. Fig. 8 of Pick et al. 1998 and Fig. 10 of Dryer et al. 1998).

4.3. Event classification

Conventional classification of SEP events had its origins in the impulsive/gradual distinction of flare microwave and soft X-ray emissions being related to parameters of corresponding energetic particle events (Cane et al. 1986, Cliver 1996, and references therein). The “two-class” picture has been recently extended by separation of each class into two subclasses (Kallenrode et al. 1992, Cliver 1996). According to the expanded classification system, there are two types of impulsive events: (Ia) impulsive events enhanced in ^3He , and (Ib) impulsive events associated with CMEs (see “Pure Impulsive” and “Mixed-Impulsive” columns in Table 2 of Cliver 1996).

How well does the 1996 July 9 event fit into this classification? The SEP event was weak, maximum proton intensity $I_p(10 \text{ MeV}) = 1.3 \times 10^{-2} \text{ cm}^{-2} \text{ sr}^{-1} \text{ s}^{-1} \text{ MeV}^{-1}$. For this reason, only few Fe ions were detected by ERNE, but the He intensity was sufficient to deduce the helium-to-proton ratio and use it for the event classification. The time integrated He/p ratio is high, $\text{He}/\text{p} = 0.12 \pm 0.02$, so that the event might be ^3He -rich (cf. Kocharov & Kocharov 1984, their Figs. 7 and 8). However, a search for ^3He led us to conclude that the event was not very rich in ^3He , the time-integrated ratio $^3\text{He}/^4\text{He} \sim 0.02$. We have searched for a temporal evolution of the ^4He -to-proton ratio. However, unlike the electron-to-proton ratio, no significant difference between the helium abundances of first and second intensity-peaks (p- and d- components) is found. It is important that the ratio of the numbers of mildly relativistic electrons to energetic protons significantly exceeds

100, the value used to distinguish impulsive events from gradual events: $I_e(0.5 \text{ MeV})/I_p(10 \text{ MeV}) \approx 7 \times 10^3$. All these facts, the impulsiveness of associated soft X-ray flare, presence of CME, high electron-to-proton and helium-to-proton ratios, but no high enhancement in ^3He , fit well properties of the subclass Ib (“Mixed-Impulsive” events according to the terminology of Cliver 1996).

We do not observe significant injection of solar energetic particles during the flare impulsive phase as well as after the CME arrival at distances $\geq 10 R_{\odot}$. Therefore, the mixed characteristics of the event do not come from the plain summation of flare accelerated and interplanetary-CME accelerated particles in consequence of their transport and registration in the interplanetary space. The properties of particle populations observed in space during this event are provided by one or several impulsive and two time-extended particle injections. Probably for this reason and also in this sense the event has mixed characteristics.

5. Conclusions

The particularly quiet conditions of particle propagation in interplanetary space make the 1996 July 9 event well suited to study the relationship between coronal energy release and the acceleration of energetic and mildly relativistic particles and their injection into interplanetary space. Comparison of *in situ* measurements of these particles and remote sensing diagnostics of coronal processes shows the following:

1. The acceleration of protons and electrons during the impulsive phase of the flare has no interplanetary counterpart observable at the SoHO site. The radio spectra provide evidence that this is because particles are mainly injected into closed structures in the low corona during this early phase of the event.
2. Mildly relativistic electrons ($E \geq 250 \text{ keV}$) and energetic protons ($E \geq 6 \text{ MeV}$) observed at 1 AU have distinctly different injection profiles. The proton injection proceeds through two successive, gradually evolving phases with different spectra, while the electron injection is mainly impulsive and accompanies only the rise of the first (p-component) proton injection. However, a minor ($\approx 25\%$) contribution of continual electron injection during the first proton rise is still possible. Electron production during the second proton rise is less than 5%.
3. The main electron injection can be traced back to a simultaneous period of electron acceleration in the corona which shows up as a broadband enhancement of radio emission from a few GHz to some tens of MHz. This occurs in and above the flaring active region. Escaping electron streams are traced by the second hectometric to kilometric type III burst group.
4. A coronal shock wave traced by its decimetric-to-metric type II radio emission accelerates the electrons that emit the radio burst, as well as electrons producing the first hectometric type III group. They have no significant counterpart in near-Earth electrons.

5. The p-component proton injection, which proceeds during about 1.5 hours after the flare onset, has a globally similar time profile as the metric-decametric (type IV) radio continuum which is related to the large scale reconfiguration of the corona in the course of the CME lift-off.
6. The subsequent softer, but more energetic d-component proton injection evolves without a signature of correlated changes in the middle corona. We suggest that the delayed acceleration is driven by the CME. The shock acceleration cannot be ruled out, but there is no positive evidence for the interplanetary shock in the event.
7. Studies of SEP genesis should not be reduced to resolving an alternative “impulsive flare acceleration *vs.* interplanetary CME-driven shock acceleration”, but should also comprise coronal acceleration at a global scale between the flare and the interplanetary CME, especially an acceleration related to reconfiguration of the solar corona during the CME development.

Acknowledgements. We are grateful to the colleagues who supplied data for this study: H. Aurass (Potsdam), E. Esagawa (Hiraiso), M. Karlický (Ondřejov), S. Krucker (Wind 3Dp experiment, Berkeley) and A. Magun (Berne). Investigations of the ERNE team are supported by the Academy of Finland. The Nançay Radio Observatory is funded by the French Ministry of Education, the CNRS and the Région Centre. The COMPTEL project is supported by NASA under contract NAS5-26645, by the German government through the DLR under grant 50 QV 90968, and by the Netherlands Organization for Scientific Research (NWO).

Appendix A: interplanetary transport model

A comprehensive description of fitting proton anisotropy data for the SEP event and corresponding description of the interplanetary transport model are given in a separate paper (Kocharov et al. 1999b). In what follows we mainly explain definitions and parameter values for the model.

To deduce electron injection scenario, interplanetary mean free path should be determined in the electron rigidity range. However, electron anisotropy data are not available. For this reason, the following method has been employed. The late phase of the relativistic electron event (Fig. 3) looks like a diffusion decay tail. The observed decay rate corresponds to the near-Earth radial mean free path parameter $\Lambda_0^{(e)} = 0.13$ AU for 0.4 MeV electrons. This interpretation implies a rather isotropic electron distribution after the intensity maximum. An abrupt change of the interplanetary magnetic field direction gave us an opportunity to verify this point. Interplanetary magnetic field direction abruptly changed at 12:50 UT by more than 70° (Torsti et al. 1997), so that electron sampling into the narrow view cone of COSTEP could be strongly affected if electron flux was as anisotropic as the proton flux was. However, only a minor change in the electron count rate was observed (marked with vertical line *B* in Fig. 3), being consistent with our estimate $\Lambda_0^{(e)} = 0.13$ AU.

While the simplest model with exactly constant radial mean free path fits the electron event decay, the expected shape of the

rising portion of the intensity curve is more rounded than the observed one. For this reason, we have adjusted the interplanetary transport model by choosing a constant parallel mean free path between Sun and Earth, whereas the constant radial mean free path is still employed beyond the Earth’s orbit.

To obtain a precise fit to the observed proton angular distribution (Torsti et al. 1997), we introduced a composite scattering model where conventional pitch angle diffusion is supplemented with a large angle scattering. The large angle scattering is modeled as Small time-Step Isotropizations (similar to the SSI model by Kocharov et al., 1998). The scattering frequency correspondingly comprises two terms: $\nu = \nu_D + \nu_L$, where two scattering processes are suggested: (i) pitch angle diffusion with corresponding partial mean free path Λ_D , and (ii) small-chance isotropizations with partial mean free path Λ_L ,

$$\Lambda_D = \frac{3V}{8} \int_{-1}^1 \frac{1 - \mu^2}{\nu_D} d\mu, \quad \Lambda_L = \frac{V}{\nu_L}. \quad (\text{A.1})$$

We have adopted the following parametrization for the partial mean free paths:

$$\Lambda_L = \frac{\Lambda_0}{f \cos^2 \Psi}, \quad \Lambda_D = \frac{\Lambda_0}{(1 - f) \cos^2 \Psi}, \quad (\text{A.2})$$

where f designates the fraction of the large-angle scattering, Λ_0 is the radial mean free path parameter, Ψ is the interplanetary magnetic field tilt angle. Available proton anisotropy data allow us to select the best-fit parameters: $\Lambda_0 = 1.1$ AU and $f = 0.85$.

Notes added in proof:

1). The steep rise of proton intensities observed at 11:50 UT (Fig. 5), with no change in the pitch-angle distribution, allows also a spatial-type interpretation. That is the magnetic connection of the spacecraft was abruptly changed-over from hard to soft spectrum source. However we do not observe a similar discontinuity in electrons (Fig. 2).

2). The electron spectrum of the 9 July 1996 event reveals hardening above 2 MeV (Sierks H., Elenndt I., Dröge W., et al., 1997, Proc. 25th Internat. Cosmic Ray Conf., Durban, South Africa, 1, 297). This behaviour is commonly observed for events with impulsive X-ray emission (Dröge W., 1996, in: Ramaty R., Mandzhavidze N., Hua X.-M. (eds.), AIP Conf. Proc. 374, High Energy Solar Physica, Woodbury, New York, p. 78).

References

- Akimov V.V., Ambrož, P., Belov A.V., et al., 1996, Solar Phys. 166, 107
- Aurass H., Hofmann A., Urbarz H.-W., 1998, A&A 334, 289
- Bieber J.W., Earl J.A., Green G., et al., 1980, JGR 85, 2313
- Bothmer V., Posner A., Kunow H., et al., 1997, in: A. Wilson (ed.), Proc. 31st ESLAB Symp., ESA SP-415, Correlated Phenomena at the Sun, in: the Heliosphere and in Geospace, ESTEC, Noordwijk, The Netherlands, p. 207
- Bougeret J.-L., Zarka P., Caroubalos C., et al., 1998, GRL 25, 2513. Erratum: GRL 25, 4103
- Cane H.V., McGuire R.E., von Rosenvinge T.T., 1986, ApJ 301, 448
- Cane H.V., Sheeley N.R., Jr., Howard R.A., 1987, JGR 92, 9869

- Chupp E.L., Trottet G., Marschhäuser H., et al., 1993, *A&A* 275, 602
- Cliver E.W., 1996, in: R. Ramaty, N. Mandzhavidze, X.-M. Hua (eds.), *AIP Conf. Proc.* 374, High Energy Solar Physics, Woodbury, New York, p. 45
- Cliver E.W., Forrest D.J., Cane H.V., et al., 1989, *ApJ* 343, 953
- Debrunner H., Lockwood J.A., Barat C., et al., 1997, *ApJ* 479, 997
- Dryer M., Andrews M.D., Aurass H., et al., 1998, *Solar Phys.* 181, 159
- Hucke S., Kallenrode M.-B., Wibberenz G., 1992, *Solar Phys.* 142, 143
- Kahler S.W., 1982, *ApJ* 261, 710
- Kahler S., 1994, *ApJ* 428, 837
- Kallenrode M.-B., Wibberenz G., 1991, *ApJ* 376, 787
- Kallenrode M.-B., Cliver E.W., Wibberenz G., 1992, *ApJ* 391, 370
- Karlický M., 1998, *A&A* 338, 1084
- Kerdraon A., Delouis J.-M., 1997, in: Trottet G. (ed.), *Lecture Notes in Physics* 483, Coronal Physics from Radio and Space Observations. Berlin: Springer, p. 192
- Klassen A., Karlický M., Aurass H., Jiříčka, K. 1999, *Solar Phys.* 188, 141
- Klein K.-L., Chupp E.L., Trottet G., et al., 1999, *A&A* 348, 271
- Kocharov L.G., Kocharov G.E., 1984, *Space Sci. Rev.* 38, 98
- Kocharov L.G., Lee J.W., Zirin H., et al., 1994, *Solar Phys.* 155, 149
- Kocharov L.G., Torsti J., Laitinen T., et al., 1997, *Solar Phys.* 175, 785
- Kocharov L., Vainio R., Kovaltsov G.A., et al., 1998, *Solar Phys.* 182, 195
- Kocharov L., Torsti J., Teittinen M., Laitinen T., 1999a, *Proc. 26th Internat. Cosmic Ray Conf.*, Salt Lake City, 6, 236
- Kocharov L., Torsti J., Laitinen T., Teittinen M., 1999b, *Solar Phys.* 190, 295
- Krucker S., Larson D.E., Lin R.P., Thompson B.J., 1999, *ApJ* 519, 864
- Lee J.W., Gary D.E., Zirin H., 1994, *Solar Phys.* 152, 409
- Lin R.P., Anderson K.A., Ashford S., et al., 1995, *Space Sci. Rev.* 71, 125
- Maia D., Vourlidas A., Pick M., et al., 1999, *JGR* 104, 12507
- Mann G., Aurass H., Klassen A., et al., 1997, in: A. Wilson (ed.), *Proc. 5th SOHO Workshop*, ESA SP-404, The Corona and Solar Wind Near Minimum Activity, ESTEC, Noordwijk, The Netherlands, p. 543
- Mann G., Jansen F., MacDowall R.J., et al., 1999, *A&A* 348, 614
- Manoharan P.K., van Driel-Gesztelyi L., Pick M., et al., 1996, *ApJ* 468, L73
- Marschhäuser H., Rieger E., Kanbach G., 1994, in: J.M. Ryan, W.T. Vestrand (eds.), *High-Energy Solar Phenomena—A New Era of Spacecraft Measurements*, AIP Conf. Proceedings 294, New York, p. 171
- Miller J.A., Cargill P.J., Emslie A.G., et al., 1997, *JGR* 102, 14631
- Müller-Mellin R., Kunow H., Fleissner V., et al., 1995, *Solar Phys.* 195, 162, 483
- Pick M., Maia D., Kerdraon A., et al., 1998, *Solar Phys.* 181, 455
- Ramaty R., Mandzhavidze N., Kozlovsky B., Skibo J.G., 1993, *Adv. Space Res.* 13(9), 275
- Raoult A., Pick M., Dennis B.R., Kane S.R., 1985, *ApJ* 299, 1027
- Reames D.V., 1999, *Space Sci. Rev.* 90, 413
- Schönfelder V., Aarts H., Bennett K., et al., 1993, *ApJS* 86, 657
- Solar Geophysical Data*, 1996, 624-I, 629-II
- Stewart R.T., Magun A., 1980, *Proc. Astron. Soc. of Australia* 4, 53
- Torsti J., Valtonen E., Lumme M., et al., 1995, *Solar Phys.* 162, 505
- Torsti J., Kocharov L.G., Vainio R., et al., 1996, *Solar Phys.* 166, 135
- Torsti J., Laitinen T., Vainio R., et al., 1997, *Solar Phys.* 175, 771
- Torsti J., Anttila A., Kocharov L., et al., 1998, *GRL* 25, 2525
- Torsti J., Kocharov L., Teittinen M., Thompson B.J., 1999, *ApJ* 510, 460